small
NANO MICRO
www.small-journal.com

Confined Assembly of Hollow Carbon Spheres in Carbonaceous Nanotube: A Spheres-in-Tube Carbon Nanostructure with Hierarchical Porosity for High-Performance Supercapacitor

*Ze Chen, Sunjie Ye, Stephen D. Evans, Yuanhang Ge, Zhifeng Zhu, Yingfeng Tu, and Xiaoming Yang**

Carbonaceous nanotubes (CTs) represent one of the most popular and effective carbon electrode materials for supercapacitors, but the electrochemistry performance of CTs is largely limited by their relatively low specific surface area, insufficient usage of intratube cavity, low content of heteroatom, and poor porosity. An emerging strategy for circumventing these issues is to design novel porous CT-based nanostructures. Herein, a spheres-in-tube nanostructure with hierarchical porosity is successfully engineered, by encapsulating heteroatom-doping hollow carbon spheres into one carbonaceous nanotube (HCSs@CT). This intriguing nanoarchitecture integrates the merits of large specific surface area, good porosity, and high content of heteroatoms, which synergistically facilitates the transportation and exchange of ions and electrons. Accordingly, the as-prepared HCSs@CTs possess outstanding performances as electrode materials of supercapacitors, including superior capacitance to that of CTs, HCSs, and their mixtures, coupled with excellent cycling life, demonstrating great potential for applications in energy storage.

1. Introduction

To meet the increasing demand of advanced storage devices with high capacity and long cycling life, there has been intensive research on carbon-based supercapacitors due to their high power density, low weight, very fast charging/discharging kinetics, long cycling life, and excellent stability.[1–3] Various carbonaceous materials, such as graphene,[4] activated carbons,[5] carbon fibers,[6] carbon films,[7] carbonaceous nanotubes (CTs),[8] and hollow carbon spheres (HCSs),[9] have been studied as electrode materials for supercapacitors.

Among the various carbonaceous materials studied, CTs have been widely investigated as electrode materials in supercapacitors, owing to their unique features of high charge transport capability, electrolyte accessibility, good chemical stability, large aspect ratio, and robust mechanical properties.[10–12] However, the relative low specific surface area (SSA, typically < 200 $m^2 g^{-1}$), low content of heteroatoms, limited usage of the intratube cavity, and poor porosity of CTs limit their electrochemistry performance.[13,14] Thus, it is essential to design hybrid heteroatom-doped CT-based materials that combine the advantages of CTs and porous nanostructures to achieve high-performance supercapacitance electrode. The main strategies for modifying the surface property of CTs to improve their electrochemical performance include (1) filling the tube with different types of active materials,[15] (2) modifying the wall of CTs via direct heating in air or chemical method such as oxidation by strong acid, to generate holes and heteroatoms on the wall,[16] and (3) deposition of a variety of electrochemically active materials on the CTs surface.[17] These strategies have improved the energy density storage ability of CTs, but were accompanied with the following issues: filling the tube impairs the charge transport capability, the modification of the wall of CTs is apt to bring about uneven distribution of pores as well as inhomogeneity of the pore size, the excessive increase of surface area causes a huge decrease of the mesoporosity. Coating the CTs does not solve the problem of low usage of CT cavity.[18,19] As such, it is desirable to design a simple and effective CT-based structure, which not only exhibits

Z. Chen, Y. H. Ge, Z. F. Zhu, Prof. Y. F. Tu, Prof. X. M. Yang
State and Local Joint Engineering Laboratory for Novel Functional Polymeric Materials Suzhou Key Laboratory of Macromolecular Design and Precision Synthesis
Jiangsu Key Laboratory of Advanced Functional Polymer Design and Application Department of Polymer Science and Engineering
College of Chemistry
Chemical Engineering and Materials Science
Soochow University
Suzhou 215123, P. R. China
E-mail: yangxiaoming@suda.edu.cn
Dr. S. J. Ye, Prof. S. D. Evans
School of Physics and Astronomy
University of Leeds
Leeds LS2 9JT, UK

The ORCID identification number(s) for the author(s) of this article can be found under https://doi.org/10.1002/smll.201704015.

DOI: 10.1002/smll.201704015

improved SSA, but also maintains high charge transport capability and high electrolyte accessibility of CTs.[12] For example, Guan and co-workers fabricated 1D tube-in-tube porous hollow carbon nanotubes (small carbon nanotubes encapsulated into large carbon nanotube), which can be used as a high-rate and flexible electrode.[20] Lin et al. prepared holey carbon nanotubes by controlled air oxidation with improved energy storage performance.[21] Wei and co-workers developed graphene/carbon nanotubes composites, which displayed improved electrical conductivity for energy storage applications.[22]

Herein, we report the design and construction of a novel spheres-in-tube structure of hollow carbon spheres encapsulated in one carbonaceous nanotube (HCSs@CT). In our approach, confined assembly of SiO_2 nanoparticle (NP) in the channels of anodic aluminum oxide (AAO) leads to generation of SiO_2@AAO dual template for subsequent polypyrrole coating, followed by carbonization and template removal to form HCSs@CT. This nanoarchitecture combines several beneficial properties for application as electrodes: (1) optimized usage of intracavity of CTs for improving SSA; (2) abundant micro/meso/macropores; (3) high charge transport capability and high electrolyte accessibilities of CTs; (4) high content of doped heteroatoms resulting from our appropriate selection of carbon precursor. In particular, HCSs in this nanoarchitecture can play important roles in enhancing supercapacitor performances, due to well-defined pore structures, high surface area, good electrical conductivity, and long cycle stability.[23,24] In addition, they can effectively reduce diffusion lengths as a result of unique large void space and interconnected pores.[25] Consequently, the HCSs@CT show excellent capacitance and cycling life characteristics for the development of supercapacitors.

2. Results and Discussion

2.1. Process and Structures

The synthetic route of HCSs@CT is illustrated in **Figure 1**. First, the AAO membranes were immersed in a SiO_2 nanoparticle (NP) dispersion. With the evaporation of solvent, the SiO_2 NPs entered the cylindrical nanopores of AAO due to capillary forces and the attractive interaction between the AAO membrane and the solution of NPs.[26] Subsequently, the NPs self-assembled into a close-packed colloidal crystal structure. The obtained SiO_2@AAO structures were then immersed in $FeCl_3$ solution and dried, at 80 °C, in air. Afterward the resultant templates were used to fabricate PPy@SiO_2@AAO arrays by a facile vapor deposition method in pyrrole vapor. Subsequently, the obtained samples were carbonized at 800 °C, followed by being etched with 3 M sodium hydroxide (NaOH) and 10% hydrofluoric acid (HF) to remove the AAO and SiO_2, respectively.

The diameter of SiO_2 NPs (64, 93, and 114 nm) was adjusted to obtain different self-assembled morphologies of SiO_2@AAO (Figure S1, Supporting Information). Erickson has worked out the various packing schemes accessible by spheres within confined channels.[27] The diameter of the sphere (d_s) relative to the AAO channel diameter (d_c) can greatly influence spheres packing. In this study, by adjusting the ratio ($\alpha = d_c/d_s$), three different morphologies of SiO_2@AAO dual templates were achieved: septuple helices packing ($\alpha = 3.33$), double helical packing ($\alpha = 2.22$), and zigzag packing ($\alpha = 1.82$), as shown in Figure S2 in the Supporting Information.

Based on the three different dual templates, the resultant carbonized products also presented three morphologies. The HCSs@CT obtained with different template size were labeled as HCSs@CT-X, where X refers to the particle size of SiO_2. The corresponding scheme models of HCSs@CT were also presented in **Figure 2**a–c. All three samples exhibited ordered close-packed HCSs well encapsulated in CT (≈5.5 nm thick) to form septuple helical packing, double helical packing, and zigzag packing, respectively (Figure 2d–f). Mesopores (≈38.1 nm) were generated uniformly on the surface of HCSs@CT-60 (Figure 2g; Figure S3a, red dotted line, Supporting Information). For HCSs@CT-90 (Figure 2h,i) and HCSs@CT-110 (Figure S3b,c, Supporting Information), the pore size increased to ≈52.4 and ≈68.5 nm, respectively, which represented well-defined macroporous structures. These meso/macropores can serve as channels for the penetration of electrolytes, and hence enhancing the supercapacitor performance, which will be

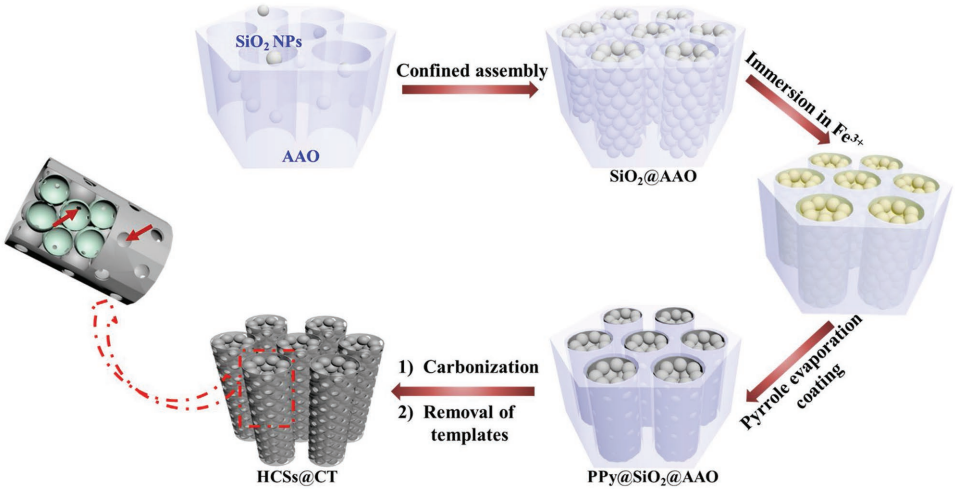

Figure 1. Schematic illustration of the production of HCSs@CT with the assistance of the dual template formed by confined assembly. In the enlarged view of HCSs@CT, meso/macropores exist between the interconnection of HCSs, and the connection of CT and HCSs (green spheres show the internal circumstances of HCSs).

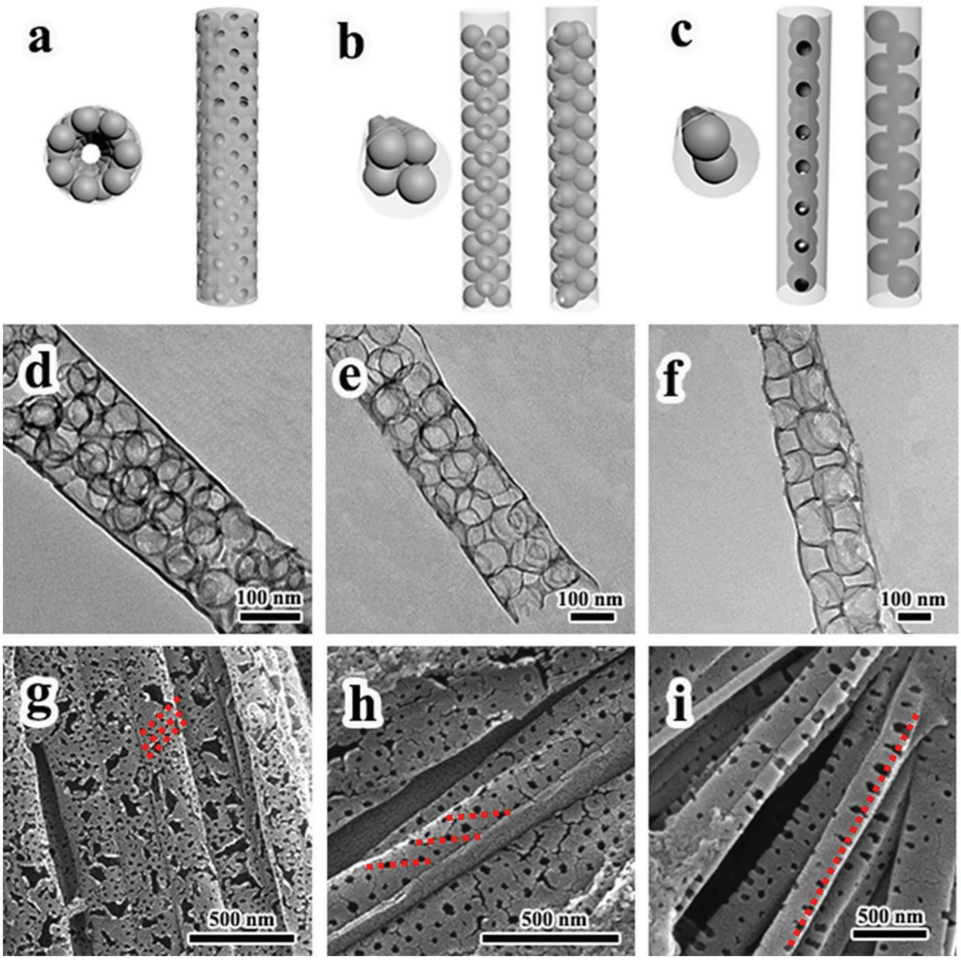

Figure 2. Schematics of a) HCSs@CT-60, b) HCSs@CT-90, and c) HCSs@CT-110. SEM and TEM images d,g) show HCSs@CT-60 with mesopores on the CT surface shown as red dotted line; e,h) show HCSs@CT-90 (macropores on the CT surface shown as red dotted line); f,i) show HCSs@CT-110 (macropores on the CT surface indicated by red dotted line).

discussed further below. The extensive pore structures of the HCSs@CT can also greatly increase the surface area, which is also crucial for supercapacitance.[28]

Due to the same preparation method for each kind of HCSs@CT-X, only the morphology of HCSs@CT-60 is discussed in detail. **Figure 3**a shows a large bundle of carbon nanotubes with the length of ≈45 µm. The resultant HCSs@CT-60 are arranged in regular arrays and lead to abundant mesopores on the CT surface, resulting from the ordered close-packed colloidal crystal structure (Figure 3b). At higher magnification, structural defects were observed (Figure 3b, red circle), caused by the packing faults of SiO_2 NPs, as is confirmed by Figure 3c.[26] Transmission electron microscope (TEM) and high resolution transmission electron microscope (HRTEM) showed structural details about porous structures following pyrolysis of HCSs@CT-60. As shown in Figure 3c,d, HCSs@CT-60 displayed abundant mesopores (white arrows), attributable to the interconnection of HCSs and the connection of CT and HCSs. This mesoporous structure is considered to provide unimpeded channels for ion transport. In situ evaluation of the elements distribution by elemental mapping with TEM revealed that carbon, nitrogen, and oxygen atoms exist homogeneously in the HCSs@CT-60 (Figure 3e–h).

2.2. Chemical Structures and Compositions

X-ray photoelectron spectroscopy (XPS) (**Figure 4** and Figure S4, Supporting Information) analysis was performed to examine the chemical compositions of all the samples. As shown in Figure 4a, C1s, N1s, and O1s existed in all the three samples, agreeing well with the result of elemental mapping with TEM (Figure 3e–h). Nitrogen and oxygen have originated mainly from PPy and SiO_2@AAO templates, and are expected to contribute to high capacitance as heteroatoms.[24] Moreover, the abundance of nitrogen can improve the conductivity, which also contributes to the enhancement of capacitance performance. The high-resolution C1s spectrum of the HCSs@CT-60 was assigned to six peaks which included C=C, C−C, C−N, C−O, C=O, and O=C−O (Figure S4a, Supporting Information).[29] The high-resolution N1s spectra of the three samples were deconvoluted into four peaks: 398.5 ± 0.2, 399.9 ± 0.1, 401.1 ± 0.2, and 403.2 ± 0.8 eV (Figure 4b), respectively, corresponding to pyridinic N, pyrrolic N, graphitic N, and pyridinic N^+-O^- groups.[30] Among them, graphitic N and pyridinic N, which are electrocatalytically active, account for more than 70% of all nitrogen atoms. According to the XPS results, a

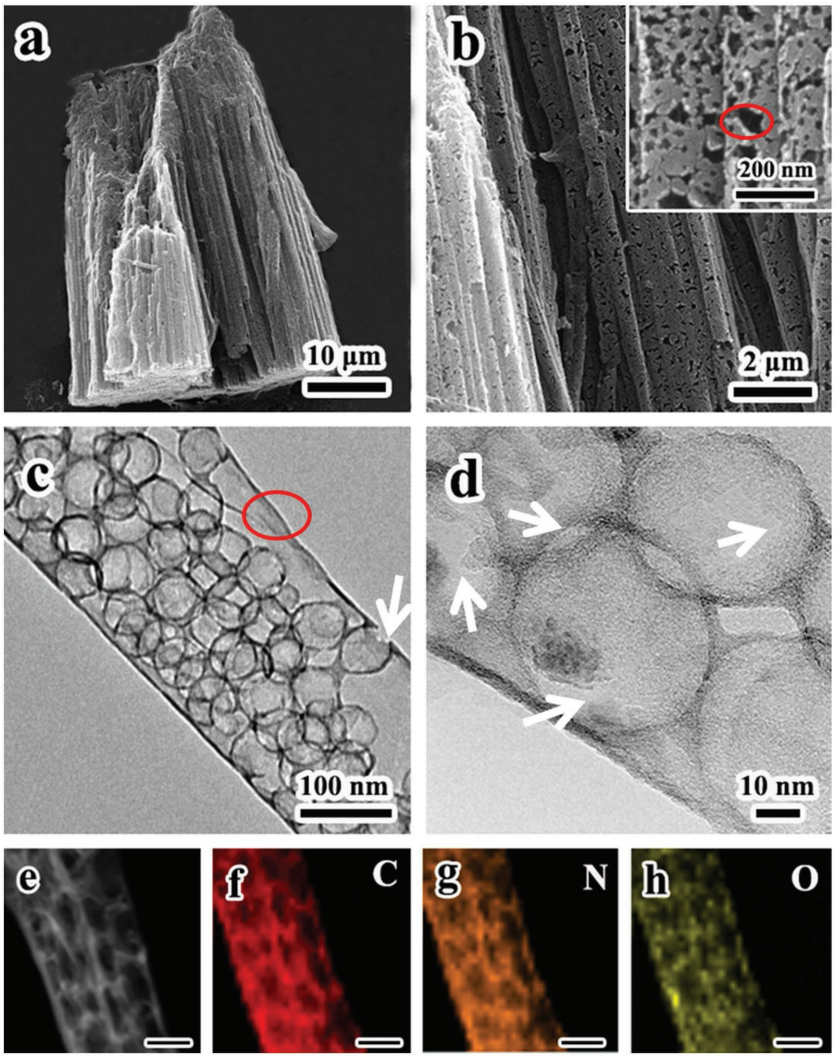

Figure 3. SEM images of HCSs@CT-60: a) Low-magnification image, b) high-magnification image showing obvious defects (red circle); c) TEM images of HCSs@CT-60 showing obvious mesopores (white arrow) and structural defects (red circle); d) HRTEM image showing abundant mesopores on the surface (white arrows); EDX mapping of HCSs@CT-60: e) STEM image; f) carbon-, g) nitrogen-, h) oxygen-mapping (scale bar: 100 nm).

possible chemical structure of HCSs@CT containing N and O functional groups is proposed in Figure S4b in the Supporting Information.

The percentage of all elements in these samples was measured and given in **Table 1**. It can be seen that heterogeneity (N + O) of all HCSs@CT samples reaches ≈12%, indicating that the nitrogen-enriched precursor and appropriate carbonization method used in this work can introduce abundant nitrogen- and oxygen-containing groups, favorable for the improvement of capacitance.[11,24]

Nitrogen sorption experiments were employed to evaluate the porous structures and SSA of HCSs@CT. The results of Brunauer–Emmett–Teller (BET) surface area, pore volume, and average pore size are summarized in Table 1. The nitrogen adsorption–desorption isotherms and corresponding pore size distribution curves of different assemblies of HCSs@CT were shown in Figure 4c,d. It can be seen from Figure 4c that all the nitrogen adsorption isotherms of HCSs@CT are of type-IV curves and exhibit a steep rise at low relative pressure ($P/P_0 < 0.001$) reflecting the abundance of microporous structures, and a steep rise at high pressure ($P/P_0 = 1$) due to the presence of macropores formed by the removal of templates. The SSA of HCSs@CT-60 (318 $m^2\ g^{-1}$) is larger than that of HCSs@CT-90 and HCSs@CT-110 (Table 1), consistent with septuple helical packing of HCSs. The porosity curves of the three samples all possessed peak from 0.81 to 100 nm, which suggest typical micro/meso/macroporous structures. The presence of micro/mesopore with the size from 0.81 to 15 nm may result from the pyrolysis of PPy.[24] In addition, all samples owned wide distribution of meso/macropores from 20 to 100 nm, and the extremums were 38.1, 52.4, and 68.5 nm, respectively, mainly attributed to the removal of SiO_2 templates (black dotted lines). The increase of pore size is consistent with the increasing SiO_2 NPs size, revealing the porosity of HCSs@CT can be controlled by the adjustment of SiO_2 template size. The hierarchical porous structures count for the electrochemical performance, since the macropores can facilitate electrolytes diffusion, and the micropores and mesopores are beneficial for the adsorption and storage of ions.

2.3. Electrochemistry Performance

Inspired by the above advantages of large SSA, high contents of heteroatoms, and abundant hierarchical porous structures of HCSs@CT, we further investigated their performance in energy storage applications. The influence of different assembled morphologies in electrochemical performance was firstly evaluated. Cyclic voltammetry (CV) curves of all the three samples scanned at 2 mV s^{-1} exhibited a quasirectangular symmetrical shape, demonstrating the existence of both electrical double-layer capacitance and pseudocapacitance, which can be attributed to large SSA, high heteroatom content, and hierarchical porous structure. Heteroatoms doping plays a very important role in the excellent storage performance. In particularly, N doping has dual effects in the composite, including improving the wettability of the composite and enhancing the electrical conductivity.[31,32] The CV curve of HCSs@CT-60 shows the largest area, suggesting the highest capacitance (**Figure 5**a). With scan rates increased to 100 mV s^{-1}, the curves still maintain quasirectangular symmetrical shapes (Figure S5a, Supporting Information). For HCSs@CT-60, scans at higher rates were conducted (Figure S5b,c, Supporting Information), demonstrating good response of the sample to high current density and high switching rates,

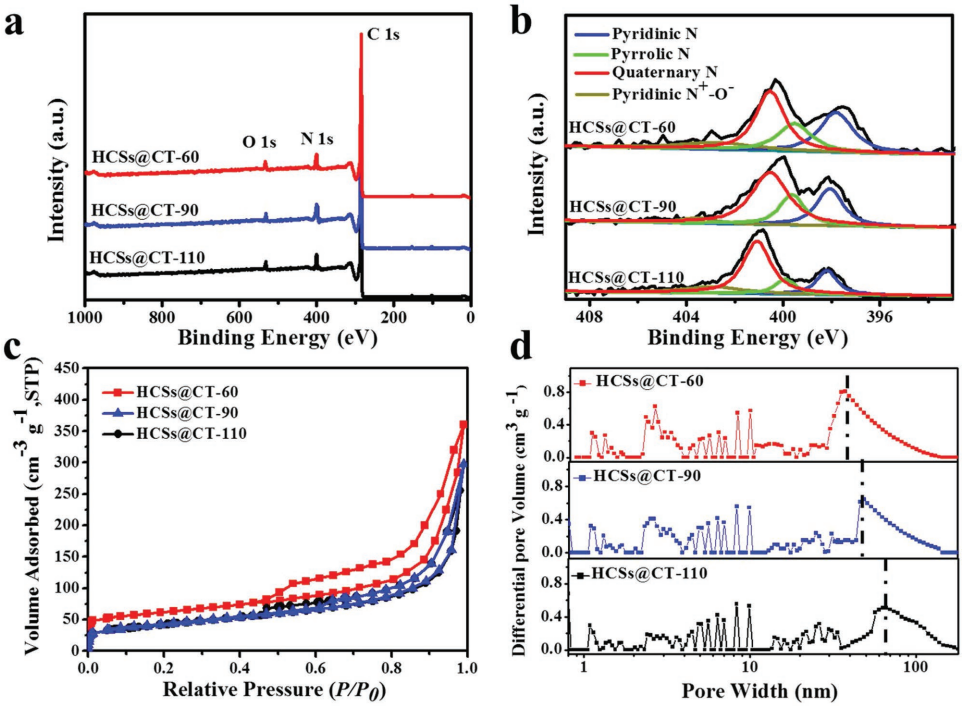

Figure 4. a) XPS survey spectra of all HCSs@CT samples; b) high-resolution N1s XPS spectra of all HCSs@CT samples; c) nitrogen adsorption/desorption isotherms of all HCSs@CT samples; d) pore size distribution of all HCSs@CT samples.

in spite of the existence of heteroatoms which are inclined to cause poor response at high current or potential due to their oxidation/reduction. The CV results are confirmed by the galvanostatic charge/discharge curves shown in Figure S5d in the Supporting Information. In addition, Figure 5b shows that specific capacitance decreases gradually with the increase of current density, which is typical for pseudocapacitive electrodes.[11] The capacitance retention of all activated samples remains above 50% even though the current density is increased to 20 A g^{-1}, suggesting the HCSs@CT are suitable for high current density applications. HCSs@CT-60 exhibited the capacitance of 235 F g^{-1} at the current density of 0.2 A g^{-1}, meanwhile maintaining 156 F g^{-1} even at the current density of 20 A g^{-1}. Since volumetric performance is also an important parameter when measuring the performance of energy storage devices, we have also calculated the volumetric capacitance. According to the obtained density of 1.16 g cm^{-3}, HCSs@CT-60 has a good volumetric capacitance up to 272 F cm^{-3}, comparable with that of other carbon electrodes in aqueous electrolytes at various particle densities (Figure S6, Supporting Information).

Table 1. Parameters of pore structures and elemental composition.

Samples	Textural properties				Chemical composition[a] [%]			
	S_{BET} [m^2 g^{-1}]	Pore size [nm]	V_{total} [cm^3 g^{-1}]	V_{micro} [cm^3 g^{-1}]	C	N	H	O
HCSs@CT-60	318	9.23	0.78	0.09	87.3	8.74	0.52	3.39
HCSs@CT-90	241	10.6	0.67	0.04	89.0	8.35	0.61	2.01
HCSs@CT-110	208	10.8	0.54	0.05	87.8	7.99	0.72	3.52

[a]Chemical composition was calculated by elemental analysis.

To further investigate the structural advantages of as-prepared HCSs@CT, we compare the electrochemistry performance of HCSs@CT-60, HCSs-60, CTs, and the mixture of HCSs-60 and CTs (mass ratio is 1:1). The specific capacitances of all the four different carbonaceous morphologies were summarized in Figure 5c. It can be found that CTs have shown the lowest capacitance (83 F g^{-1}), consistent with its low SSA and porosity (Figures S7 and S8 and Table S1, Supporting Information). The capacitance of HCSs-60 is higher than CTs, mainly ascribable to the difference of morphologies (Figure S9 and Table S2, Supporting Information). As shown in Figure S10 (Supporting Information), in contrast to HCSs encapsulated in CT, the pristine HCSs-60 exhibit partially ruptured shell, which resulted from the thin PPy shell being unable to withstand pyrolysis. More importantly, HCSs@CT-60 have shown higher capacitance than the mixture of HCSs-60 and CTs. We summarize the supercapacitance performance of carbonaceous materials with different morphologies in Table S3 in the Supporting Information. It was shown that HCSs@CT-60 displayed better performance than HCSs-60, CTs, or the mixture of HCSs-60 and CTs, demonstrating that the structural features in our spheres-in-tube nanoarchitecture synergistically led to the enhancement of electrochemical capacitance.

In addition, the unique spheres-in-tube structure of HCSs@CT-60 also performed well in promoting the transportation of ions and electrons, as confirmed in Figure 5d. HCSs@CT-60 displayed low equivalent series resistance (ESR) and charge transfer resistance (R_{ct}), which are inherited characteristics of the HCSs and CTs. The ESR of HCSs@CT-60 implied that the

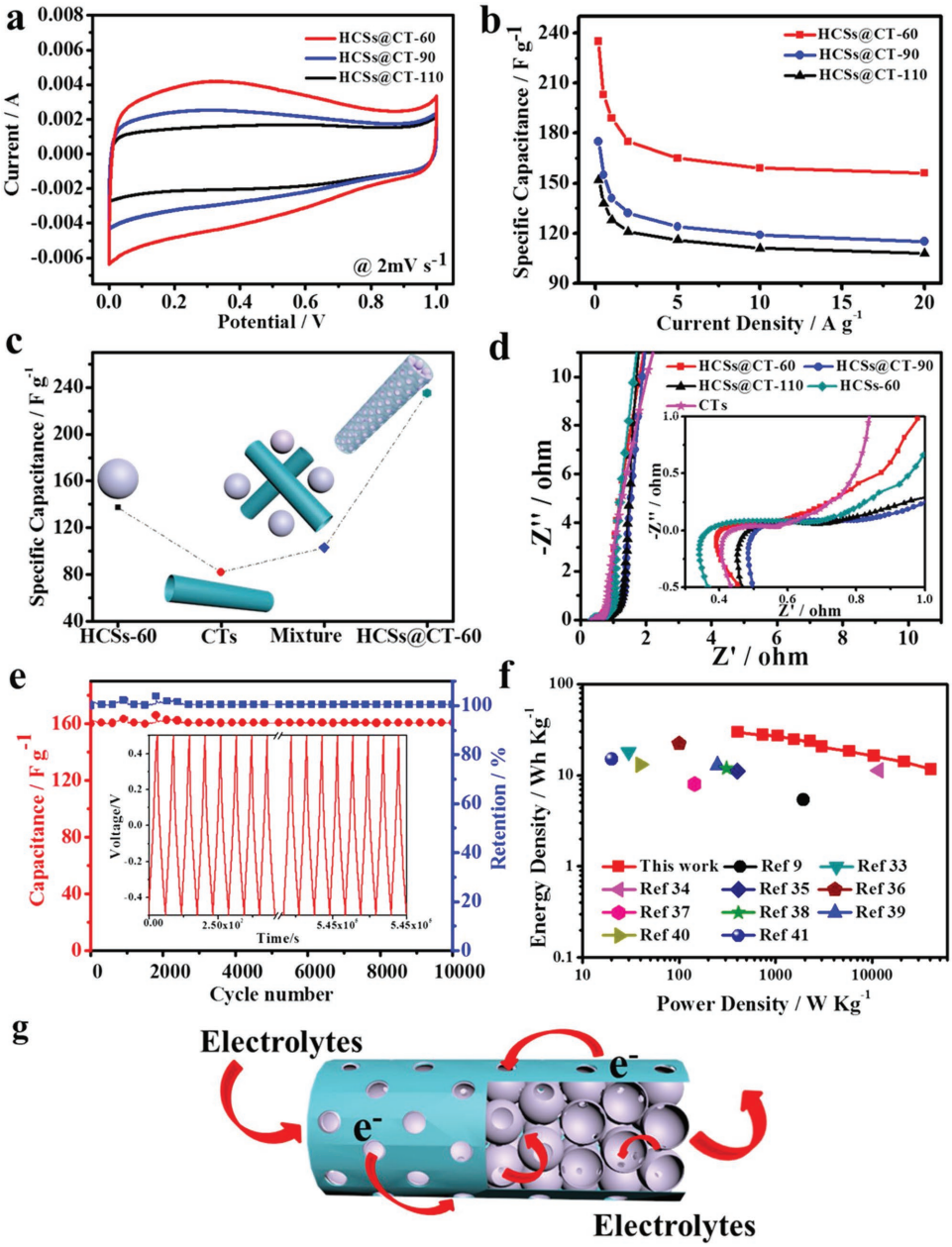

Figure 5. a) CV curves of all HCSs@CT samples at 2 mV s^{-1} (6 M KOH as electrolyte). b) Capacitance versus discharge current density from 0.2 to 20 A g^{-1}. c) Gravimetric-specific capacitance of different carbonaceous morphologies measured at 0.2 A g^{-1}. d) Nyquist plot of different carbonaceous morphologies (0.01 Hz to 100 kHz). e) Cycling life test of HCSs@CT-60 (5.0 A g^{-1} for 10 000 cycles). f) Ragone plot of carbon-based symmetric supercapacitors. g) Transport mechanism of electrons and ions in HCSs@CT.

heteroatoms play an important role in the energy storage, for being more favorable to attract ions in the electrolyte compared with that of carbon atoms. Meanwhile, the R_{ct} of HCSs@CT-60 is the lowest except that of CTs. This is mainly because that the unique septuple helical packing structure has a channel in the center of tube, which can effectively facilitate the transport of ions. The transport mechanism of electrons and ions in HCSs@CT-60 was shown in Figure 5g. The meso/macropores facilitate the transportation of electrons and ions, and micropores improved the storage ability of ions, leading to the synergy effect of improving the electrochemical performances.

In the cycling life test, the increase of capacitance from 100 to 103% after more than 1000 cycles has been observed, which indicates increased continuous impregnation of the electrolyte ions in the micro/mesopores of the electrode during the charge/discharge processes (Figure 5e). In addition, HCSs@CT-60 exhibited a good electrochemical stability with negligible degradation of specific capacitance after 10 000 cycles. A two-electrode cell test was used to estimate the energy density and power density, which are vital parameters for practical applications. These were calculated from the galvanostatic charge/discharge process curve using the following equations

$$C = \frac{I\Delta t}{m\Delta V} \quad (1)$$

$$E = \frac{1}{2} \times C \times (\Delta V)^2 \quad (2)$$

$$P = \frac{E}{\Delta t} \quad (3)$$

where C is the specific capacitance (F g^{-1}), I is the current (A) during scanning, Δt represents current drain time of discharging (s), m indicates total mass of the active material (g), and ΔV is the potential window (3 V in this work). The Ragone plots in Figure 5f show the dependence of energy density on power output. It revealed that HCSs@CT-60-based supercapacitor can deliver a high energy density of 29.5 Wh kg^{-1} at the power density of 401 W kg^{-1} which is superior to that of other carbon-based supercapacitors. The improved performance can be ascribed to the synergistic effect of the high SSA, the unique hierarchical porous structure, and the abundant heteroatoms, which effectively boost the transportation and storage of ions and electrons in electrodes and at the electrode/electrolyte interface.

3. Conclusion

In summary, to improve the electrochemical performance of CNTs, we have successfully developed a spheres-in-tube nanoarchitecture of heteroatom-doped hollow carbon spheres encapsulated in carbon tubes. The fabrication strategy relies on the confined assembly of SiO_2 NPs in the channels of AAO to form dual template for PPy coating, followed by carbonization and template removal. The unique spheres-in-tube architecture provides large SSA, high heteroatom content, and hierarchical porous structure, which in synergy lead to the significant improvement of the energy storage performance. As a result, the supercapacitor based on HCSs@CT-60 has exhibited a specific capacitance of 235 F g^{-1} at 0.2 A g^{-1} and 156 F g^{-1} at 20 A g^{-1} in 6 M KOH solution, much higher than that of HCSs, CTs, or even the mixture of HCSs and CTs prepared under the same conditions. In addition, the HCSs@CT-60 also exhibit excellent electrochemical stability and maintain high charge transport capability after 10 000 cycles. The resultant architectures of high heterogeneity and hierarchy hold great promise for a variety of other applications such as catalysis, energy conversion, and so on. In addition, the structure of meso/macropores enables effective encapsulation of active materials into cavities, and more potential applications are being explored.

4. Experimental Section

Materials: AAO membranes with pore size of 200 ± 16.7 nm were purchased from Puyuan Nanotech, Co., Ltd., China. These membranes are freestanding disks with a diameter of 25 mm and a thickness of 60 µm, with double-pass channels. Pyrrole (Aldrich, 99%) was used after distillation under reduced pressure and stored under argon atmosphere at 4 °C. Ultrapure water (18.2 MΩ·cm^{-1}) was used directly from Milli-Q water system. Kimwipes airlaid papers were purchased from Kimberly-Clark Worldwide, Inc. Tetra-ethyl-orthosilicate (TEOS, A.R.), ammonia hydroxide (NH_4OH, 28%, A.R.), anhydrous ferric chloride ($FeCl_3$, 98%), hydrofluoric acid (HF, A.R.), and 200 proof ethanol (EtOH, A.R.) were purchased from Sinopharm Chemical Reagent Co., Ltd., which were used as received.

Preparation of SiO_2: SiO_2 latex with different diameters were prepared by the Stöber–Fink–Bohn method.[42] Three different particle sizes were prepared: 64.1 ± 3.25 nm, 93.3 ± 4.54 nm, and 114.2 ± 4.68 nm, as determined by dynamic light scattering.

Preparation of SiO_2@AAO Dual Templates: Firstly, the AAO membrane was treated to be hydrophilic by oxygen plasma followed by immersion in 10 mL of SiO_2 NPs in ethanol (≈2 mg·mL^{-1}). Slow evaporation of ethanol allowed the SiO_2 NPs to enter the nanopores of the membrane due to capillary forces, followed by drying in vacuum for 2 h. The excess SiO_2 NPs on the AAO surface were gently wiped away using Kimwipes.

Preparation of HCSs@CT: The SiO_2@AAO dual templates were immersed in 0.2 M ethanol solution of $FeCl_3 \cdot 6H_2O$ for about 30 min, followed by drying at 80 °C for 1 h. Then the AAO template was horizontally placed in a chamber. Pyrrole monomer was introduced into the chamber through a pipe and evaporated slowly at 37 °C. The whole vapor phase deposition process was carried out for 5 d. The obtained samples were further carbonized to fabricate HCSs@CT in a quartz tubular furnace under nitrogen atmosphere. The sample was gradually heated up to 800 °C, at a heating rate of 5 °C min^{-1}, then kept at 800 °C for 1.5 h, and then cooled to room temperature. Finally, the samples were immersed in 3 M NaOH and 10% HF to remove AAO and SiO_2, respectively.

Preparation of CTs: The preparation procedure of CTs followed the preparation of HCSs@CT except for the omission of SiO_2 into the AAO. In addition, the obtained samples were only subject to immersion in 3 M NaOH to remove AAO.

Preparation of HCSs: SiO_2 powder (0.5 g) was immersed in 0.2 M ethanol solution of $FeCl_3 \cdot 6H_2O$ for about 30 min, followed by centrifuge and drying at 80 °C for 1 h. Then the SiO_2 was horizontally placed in a chamber. The following procedures of polypyrrole deposition and carbonization are as the same as preparation of HCSs@CT. Finally, the samples were immersed in 10% HF to remove SiO_2.

Characterization: Scanning electron microscopy (SEM) images were obtained with Quanta 400 FEG. TEM, scanning transmission electron microscope (STEM) imaging, and energy dispersive X-Ray (EDX) mapping were performed on a FEI Tecani G2 F20 S-TWIN. XPS measurements were performed using an ESCALAB 250 instrument (Thermo Electron) with Al Kα radiation. Element analysis was performed using Vario EL cube. The nitrogen sorptions of the samples were measured at 77 K using NOVA 2000 (Micromeritics ASAP 2020).

Electrochemical Measurements: The electrochemical performances of as-prepared samples were evaluated in a three-electrode configuration. The samples with carbon black and polytetrafluoroethylene binder (8:1:1) were mixed in water. A three-electrode setup was used for all electrochemical measurements except power density and energy density. The measurements were carried out on a CHI660E electrochemical workstation in 6 M KOH and 1 M H_2SO_4 aqueous electrolytes at room temperature. The symmetrical two-electrode testing coin supercapacitor was manufactured, where the two electrodes were separated by a filter paper soaked with 1 M Na_2SO_4 electrolyte. The working electrode was prepared by mixing the HCSs@CT with polyvinylidene fluoride and carbon black (8:1:1) in *N*-methyl 2-pyrrolidone to form a homogeneous slurry. The typical mass loading on one electrode was around 2.4 mg cm^{-2}, and the thickness of electrode was controlled to be about 37 µm. The electrochemical characterizations were performed on a CHI660E electrochemical workstation at room temperature.

Supporting Information

Supporting Information is available from the Wiley Online Library or from the author.

Acknowledgements

The authors gratefully acknowledge the financial support from the National Natural Science Foundation of China (Nos. 21104050 and 11604045), China Postdoctoral Science Foundation (2013M541715 and 2014T70541), a Project Funded by the Priority Academic Program Development of Jiangsu Higher Education Institutions (PAPD), and the Fundamental Research Funds for the Central Universities and Shanghai Science and Technology Commission (16PJ1400100, 17ZR1440000, and 17JC400700), and EPSRC (EP/P023266/1). The data associated with this article are available from University of Leeds https://doi.org/10.5518/328.

Conflict of Interest

The authors declare no conflict of interest.

Keywords

carbon nanostructures, confined assembly, heteroatoms doping, spheres-in-tube, supercapacitors

Received: November 16, 2017
Revised: January 25, 2018
Published online: March 26, 2018

[1] A. Burke, *J. Power Sources* **2000**, *91*, 37.
[2] J. B. Goodenough, *Energy Storage Mater.* **2015**, *1*, 158.
[3] S. Chu, A. Majumdar, *Nature* **2012**, *488*, 294.
[4] R. Raccichini, A. Varzi, S. Passerini, B. Scrosati, *Nat. Mater.* **2015**, *14*, 271.
[5] M. Sevilla, P. Valle-Vigón, A. B. Fuertes, *Adv. Funct. Mater.* **2011**, *21*, 2781.
[6] G. Z. Sun, X. Zhang, R. Z. Lin, J. Yang, H. Zhang, P. Chen, *Angew. Chem.* **2015**, *127*, 4734; *Angew. Chem., Int. Ed.* **2015**, *54*, 4651.
[7] G. Y. Zheng, S. W. Lee, Z. Liang, H. W. Lee, K. Yan, H. B. Yao, H. T. Wang, W. Y. Li, S. Chu, Y. Cui, *Nat. Nanotechnol.* **2014**, *9*, 618.
[8] J. B. Yin, X. Xia, L. Q. Xiang, X. P. Zhao, *Carbon* **2010**, *48*, 2958.
[9] K. Wang, L. Huang, S. Razzaque, S. Jin, B. Tan, *Small* **2016**, *12*, 3134.
[10] R. H. Baughman, A. A. Zakhidov, W. A. De Heer, *Science* **2002**, *297*, 787.
[11] C. X. Guo, N. Li, L. L. Ji, Y. W. Li, X. M. Yang, Y. Lu, Y. F. Tu, *J. Power Sources* **2014**, *247*, 660.
[12] Q. L. Wei, F. Y. Xiong, S. S. Tan, L. Huang, E. H. Lan, B. Dunn, L. Q. Mai, *Adv. Mater.* **2017**, *29*, 1602300.
[13] Z. J. Fan, J. Yan, L. J. Zhi, Q. Zhang, T. Wei, J. Feng, M. L. Zhang, W. Z. Qian, F. Wei, *Adv. Mater.* **2010**, *22*, 3723.
[14] A. Afzal, F. A. Abuilaiwi, A. Habib, M. Awais, S. B. Waje, M. A. Atieh, *J. Power Sources* **2017**, *352*, 174.
[15] F. Y. Jin, S. Xiao, L. J. Lu, Y. Wang, *Nano Lett.*. **2016**, *16*, 440.
[16] C. J. Niu, J. S. Meng, X. P. Wang, C. H. Han, M. Y. Yan, K. N. Zhao, X. M. Xu, W. H. Ren, Y. L. Zhao, L. Xu, Q. J. Zhang, D. Y. Zhao, L. Q. Mai, *Nat. Commun.* **2015**, *6*, 7402.
[17] Y. M. Chen, Z. G. Lu, L. M. Zhou, Y. W. Mai, H. T. Huang, *Energy Environ. Sci.* **2012**, *5*, 7898.
[18] Y. M. Sun, R. B. Sills, X. L. Hu, Z. W. Seh, X. Xiao, H. H. Xu, W. Luo, H. Y. Jin, Y. Xin, T. Q. Li, Z. L. Zhang, J. Zhou, W. Cai, Y. H. Huang, Y. Cui, *Nano Lett.* **2015**, *15*, 3899.
[19] S. Zhang, Y. Y. Shao, Y. Z. Gao, G. Y. Chen, Y. H. Lin, G. P. Yin, *J. Power Sources* **2011**, *196*, 9955.
[20] Y. Zhao, W. L. Wu, J. X. Li, Z. C. Xu, L. H. Guan, *Adv. Mater.* **2014**, *26*, 5113.
[21] Y. Lin, M. R. Funk, C. J. Campbell, J. W. Kim, X. G. Han, S. D. Lacey, H. Xie, L. B. Hu, J. W. Connell, *Adv. Funct. Mater.* **2017**, *27*, 1700762.
[22] H. J. Peng, J. Q. Huang, M. Q. Zhao, Q. Zhang, X. B. Cheng, X. Y. Liu, W. Z. Qian, F. Wei, *Adv. Funct. Mater.* **2014**, *24*, 2772.
[23] J. Liu, N. P. Wickramaratne, S. Z. Qiao, M. Jaroniec, *Nat. Mater.* **2015**, *14*, 763.
[24] Z. Chen, R. Cao, Y. H. Ge, Y. F. Tu, Y. Xia, X. M. Yang, *J. Power Sources* **2017**, *363*, 356.
[25] Y. B. Yin, J. J. Xu, Q. C. Liu, X. B. Zhang, *Adv. Mater.* **2016**, *28*, 7494.
[26] R. J. Liang, J. P. Xu, R. H. Deng, K. Wang, S. Q. Liu, J. Y. Li, J. T. Zhu, *ACS Macro Lett.* **2014**, *3*, 486.
[27] R. O. Erickson, *Science* **1973**, *181*, 705.
[28] Y. P. Zhai, Y. Q. Dou, D. Y. Zhao, P. F. Fulvio, R. T. Mayes, S. Dai, *Adv. Mater.* **2011**, *23*, 4828.
[29] C. Zhang, W. Lv, Y. Tao, Q. H. Yang, *Energy Environ. Sci.* **2015**, *8*, 1390.
[30] Z. X. Xu, X. D. Zhuang, C. Q. Yang, J. Cao, Z. Q. Yao, Y. P. Tang, J. Z. Jiang, D. Q. Wu, X. L. Feng, *Adv. Mater.* **2016**, *28*, 1981.
[31] L. Li, Q. F. Zhong, N. D. Kim, G. D. Ruan, Y. Yang, C. T. Gao, H. L. Fei, Y. L. Li, Y. S. Ji, J. M. Tour, *Carbon* **2016**, *105*, 260.
[32] T. Q. Lin, I. W. Chen, F. X. Liu, C. Y. Yang, H. Bi, F. F. Xu, F. Q. Huang, *Science* **2015**, *350*, 1508.
[33] A. F. Arif, Y. Kobayashi, R. Balgis, T. Ogi, H. Iwasaki, K. Okuyama, *Carbon* **2016**, *107*, 11.
[34] Q. Wang, J. Yan, Y. Wang, G. Ning, Z. J. Fan, T. Wei, J. Cheng, M. L. Zhang, X. Y. Jing, *Carbon* **2013**, *52*, 209.
[35] C. Liu, J. Wang, J. S. Li, M. L. Zeng, R. Luo, J. Y. Shen, X. Y. Sun, W. Q. Han, L. J. Wang, *ACS Appl. Mater. Interfaces* **2016**, *8*, 7194.
[36] Z. Lei, J. T. Zhang, X. S. Zhao, *J. Mater. Chem.* **2012**, *22*, 153.
[37] L. F. Chen, X. D. Zhang, H. W. Liang, M. G. Kong, Q. F. Guan, P. Chen, Z. Y. Wu, S. H. Yu, *ACS Nano* **2012**, *6*, 7092.
[38] Q. Wang, J. Yan, Y.B. Wang, T. Wei, M. L. Zhang, X. Y. Jing, Z. J. Fan, *Carbon* **2014**, *67*, 119.
[39] N. Xiao, H. T. Tan, J. X. Zhu, L. P. Tan, X. H. Rui, X. C. Dong, Q. Y. Yan, *ACS Appl. Mater. Interfaces* **2013**, *5*, 9656.
[40] Y. Tao, X. Xie, W. Lv, D. M. Tang, D. B. Kong, Z. H. Huang, H. Nishihara, T. Ishii, L. Baohua, D. Golberg, F. Y. Kang, T. Kyotani, Q. H. Yang, *Sci. Rep.* **2013**, *3*, 2975.
[41] E. Raymundo-Pinero, M. Cadek, F. Beguin, *Adv. Funct. Mater.* **2009**, *19*, 1032.
[42] W. Stöber, A. Fink, E. Bohn, *J. Colloid Interface Sci.* **1968**, *26*, 62.